

# Atomistic Observation of the Local Phase Transition in MoTe<sub>2</sub> for Application in Homojunction Photodetectors

Yalan Wang, Miao Zhang, Zhongying Xue, Xinqian Chen, Yongfeng Mei, Paul K. Chu, Ziao Tian, Xing Wu,\* and Zengfeng Di\*

Direct atomic-scale observation of the local phase transition in transition metal dichalcogenides (TMDCs) is critically required to carry out in-depth studies of their atomic structures and electronic features. However, the structural aspects including crystal symmetries tend to be unclear and unintuitive in real-time monitoring of the phase transition process. Herein, by using in situ transmission electron microscopy, information about the phase transition mechanism of MoTe<sub>2</sub> from hexagonal structure (2H phase) to monoclinic structure (1T' phase) driven by sublimation of Te atoms after a spike annealing is obtained directly. Furthermore, with the control of Te atom sublimation by modulating the hexagonal boron nitride (h-BN) coverage in the desired area, the lateral 1T'-enriched MoTe<sub>2</sub>/2H MoTe<sub>2</sub> homojunction can be one-step constructed via an annealing treatment. Owing to the gradient bandgap provided by 1T'-enriched MoTe<sub>2</sub> and 2H MoTe<sub>2</sub>, the photodetector composed of the 1T'-enriched MoTe<sub>2</sub>/2H MoTe<sub>2</sub> homojunction shows fast photoresponse and ten times larger photocurrents than that consisting of a pure 2H MoTe<sub>2</sub> channel. The study reveals a route to improve the performance of optoelectronic and electronic devices based on TMDCs with both semiconducting and semimetallic phases.

phases in TMDCs have significant influence on the physicochemical properties of the materials.<sup>[4,5]</sup> For example, the hexagonal 2H MoTe<sub>2</sub> has semiconducting properties, whereas the monoclinic 1T' MoTe<sub>2</sub> is typically semimetallic and the phase transition from 2H to 1T' in MoTe<sub>2</sub> results in bandgap shrinkage from  $\approx 1$  eV to  $\approx 60$  meV.<sup>[6,7]</sup> More importantly, the structural phase transition in TMDCs provides a unique approach to modulate the materials properties to cater to different types of contacts, transistors, resistive memories, and even superconductors.<sup>[8–10]</sup> To explore the physics of phase transition, efforts have been made on atomic-scale observation of TMDCs with various phase structures by transmission electron microscopy (TEM).<sup>[11–13]</sup> However, the atomic features in different phases of TMDCs are generally unraveled indirectly via ex situ TEM, leaving the structural evolution and underlying mechanism unclear.<sup>[14]</sup> Besides, real-time observation


## 1. Introduction

2D layered transition metal dichalcogenides (TMDCs) comprising a layer of transition-metal atoms sandwiched between two layers of chalcogen atoms consist of numerous crystal phases with distinct symmetries such as the hexagonal structure (2H phase) and distorted octahedral or monoclinic structure (1T' phase).<sup>[1–3]</sup> The transitions between these different

of subtle changes in specimen under various experimental conditions are crucially required due to the instability of most TMDCs, which are generally easily oxidized, and easily decomposed at high temperatures.<sup>[15,16]</sup> Thereafter, in situ atomic-scale observation is developed to capture the specimen's changing behavior instantly before damage occurs. Phase transition from 2H to 1T' phase in MoTe<sub>2</sub> has been achieved by applying laser or strain,<sup>[1,17]</sup> nevertheless, the atomic structural

Y. Wang, M. Zhang, Z. Xue, Z. Tian, Z. Di  
State Key Laboratory of Functional Materials for Informatics  
Shanghai Institute of Microsystem and Information Technology  
Chinese Academy of Sciences  
Shanghai 200050, P. R. China  
E-mail: zfdi@mail.sim.ac.cn

Y. Wang  
Center of Materials Science and Optoelectronics Engineering  
University of Chinese Academy of Sciences  
Beijing 100049, P. R. China

 The ORCID identification number(s) for the author(s) of this article can be found under <https://doi.org/10.1002/smll.202200913>.

X. Chen, X. Wu  
Shanghai Key Laboratory of Multidimensional Information Processing  
School of Communication and Electronic Engineering  
East China Normal University  
500 Dongchuan Road, Shanghai 200241, P. R. China  
E-mail: xwu@ee.ecnu.edu.cn

Y. Mei  
Department of Materials Science  
State Key Laboratory of ASIC and Systems  
Fudan University  
Shanghai 200433, P. R. China

P. K. Chu  
Department of Physics  
Department of Materials Science and Engineering  
and Department of Biomedical Engineering  
City University of Hong Kong  
Tat Chee Avenue, Kowloon, Hong Kong 999077, P. R. China

DOI: 10.1002/smll.202200913

changes during the phase transition process need to be further studied.

Phase engineering has been widely developed to modulate material properties and provide opportunities for future devices.<sup>[18,19]</sup> With the understanding of phase transition mechanism in TMDCs and the tuning of their physical properties, field-effect transistors (FETs) composed of TMDCs homojunction have been presented to effectively reducing the contact resistance between electrodes and channel materials.<sup>[20]</sup> It is believed that the reduced contact resistance attributes to the gradient bandgap concomitant with the phase transition, which is widely utilized in improving the performance of photodetector and other devices.<sup>[21,22]</sup>

Take MoTe<sub>2</sub> for example, by converting the semiconducting 2H phase to the semimetallic 1T' phase in the electrodes contacting region, the charge transfer efficiency can be regulated by constructing ohmic contacts.<sup>[23]</sup> Currently, FETs composed of TMDCs homojunction can be prepared by laser illumination, growth regulating or element doping;<sup>[1,10,24]</sup> however, a more controllable and simple method to realize the fabrication of homojunction devices is needed.

In this work, the phase transition from 2H to 1T' phase in MoTe<sub>2</sub> is observed directly by in situ heating TEM observation, presenting the atomic structure changes in MoTe<sub>2</sub> with atomic resolution. The phase transition shows a nonuniform “wagon wheel” pattern on the multilayer MoTe<sub>2</sub> arising from facilitated sublimation of Te atoms (sublimation temperature of ≈400 °C<sup>[6]</sup>), resulting in phase transition in the local area.<sup>[16,25]</sup> In addition, the seamless connection between these two phases has contributed to the excellent performance of the MoTe<sub>2</sub>-based homojunction device we constructed later in this work. Moreover, the sublimation of Te atoms is impeded by coverage of thick hexagonal Boron Nitride (h-BN) even at a high temperature. Using local phase transition engineering by patterning h-BN on MoTe<sub>2</sub>, the transition between the 2H and 1T'-enriched phases in MoTe<sub>2</sub> in the desired area can be controlled and the lateral 1T'-enriched MoTe<sub>2</sub>/2H MoTe<sub>2</sub> homojunction can be obtained by one-step annealing. Compared to the conventional 2H MoTe<sub>2</sub> devices, both the electronic and optoelectronic properties of the device with the lateral 1T'-enriched MoTe<sub>2</sub>/2H MoTe<sub>2</sub> homojunction are improved considerably. The strategy of manipulating the phase transition between 2H and 1T' of MoTe<sub>2</sub> can be further explored to prepare more complex lateral homojunctions with versatile functions.

## 2. Results and Discussion

### 2.1. In Situ TEM Observation of the Phase Transition in MoTe<sub>2</sub> Flake

For in situ TEM observation, the bulk 2H MoTe<sub>2</sub> is dispersed ultrasonically in ethanol into sheets with nanoscale thickness and then transferred onto a nanochip (supplied by Wildfire, DENS solutions Co., Ltd.) as illustrated schematically in Figure 1a. The TEM nanochip has electron transparent silicon nitride membrane windows to hold the specimen during heating, as shown in Figure S1 in the Supporting Information. To minimize the influence of electron beam irradiation, the

work voltage of high-resolution transmission electron microscopy (HR-TEM) is chosen as 80 kV. The image of pristine 2H MoTe<sub>2</sub> flake is captured at low magnification (Figure 1b) and the zoomed-in area of the dotted white box shows the atomic arrangements of 2H MoTe<sub>2</sub> clearly (Figure 1c). The corresponding fast Fourier transform (FFT) pattern of Figure 1c displays a set of sixfold diffraction spots with uniform intensities confirming good single crystalline properties (Figure 1d). To accurately monitor the phase transition process from 2H to 1T' in MoTe<sub>2</sub>, in situ spike (1 s) heating is carried out to raise the sample temperature to the target between 500 and 880 °C rapidly (details shown in Figure S2c–g, Supporting Information).<sup>[6]</sup> To prevent the sample from sublimation at high temperatures, the temperature is reset to 20 °C immediately after each heating pulse for image acquiring (heating procedure detailed in Figure S2a, Supporting Information).<sup>[26,27]</sup> The phase transition-related streaks start to appear after the 1 s spike heating at 880 °C (Figure 1e,f). The HR-TEM image in Figure 1g shows the magnified area marked by the dotted white box in Figure 1f. In addition to the pristine hexagonal symmetrical atomic structure of 2H MoTe<sub>2</sub>, there is a newly generated ribbon-shaped domain consisting of distinctive monoclinic (distorted octahedral structure) 1T' MoTe<sub>2</sub>.<sup>[28,29]</sup> Owing to the mixed 2H and 1T' phase, the FFT pattern of Figure 1g reveals two sets of diffraction patterns, as provided in Figure 1h. One set of which exhibits a sixfold symmetry arising from the initial 2H MoTe<sub>2</sub> lattice as shown in Figure 1d. While, the other set of rectangular spots suggests the occurrence of phase transition corresponding to the monoclinic crystal structure of 1T' MoTe<sub>2</sub>.<sup>[14,30,31]</sup>

Previous studies involving thermal annealing and laser-induced local heating suggest that the heating process produces sample thinning and Te sublimation, thus resulting in the phase transition from 2H to 1T' in MoTe<sub>2</sub>.<sup>[1,32,33]</sup> In our study, because of the degraded thermal conductivity in the high vacuum TEM cell, local heat dissipation through MoTe<sub>2</sub> layers after a spike heating at 880 °C initiates sublimation of partial Te atoms and triggers the phase transition from 2H to 1T' as well. In fact, the role of Te sublimation on phase transition of MoTe<sub>2</sub> is evident by the reversible phase transition between 2H to 1T' in MoTe<sub>2</sub> tuned by the concentration of Te source.<sup>[14]</sup> The theoretical study suggests that the ordering of Te vacancies generated from the sublimation of Te atoms can release the strong repulsion at the interface between the two phases.<sup>[34]</sup> As the Te vacancies gathering, the significantly reduced potential barrier between 2H and 1T' phases has facilitated the phase transition.<sup>[35,36]</sup> Since the phase transition is attributed to the sublimation of Te atoms, it can be further manipulated by the coverage of h-BN in our later experiments. The newly formed ribbon-shaped 1T' MoTe<sub>2</sub> domains (Figure 1f,g) are supposed to be triggered by the “wagon wheel” patterns formed at the high temperature due to surface desorption and dissociation.<sup>[16,25]</sup> The Te atoms are apt to sublimate to generate Te vacancies at the inversion domain boundary defects, and the agglomeration of Te vacancies is responsible for the formation of the ribbon-shape phase transition domains.<sup>[16]</sup> The previous works have demonstrated that the phase transition domains are generated by the agglomeration of chalcogen vacancies at high temperature, and their special morphology is related to the crystal symmetry of the material.<sup>[37,38]</sup>

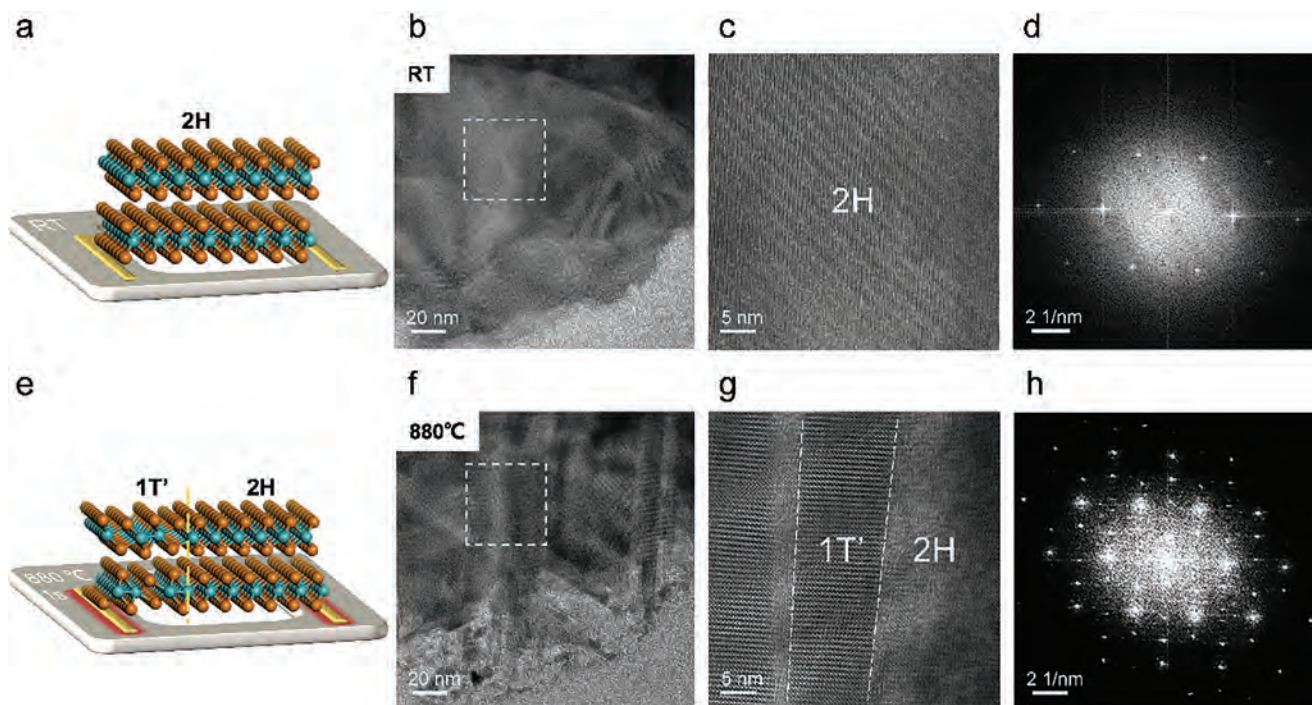


**Figure 1.** In situ TEM observation of few layer 2H MoTe<sub>2</sub> before and after 880 °C heating pulse. a) Schematic illustration of 2H MoTe<sub>2</sub> on the nanochip at room temperature. b) Low-magnification HR-TEM image of 2H MoTe<sub>2</sub> at room temperature. c) Magnified area of the dotted white box in (b) showing single-crystalline 2H MoTe<sub>2</sub> with the optimized symmetric hexagonal atomic structure. d) FFT pattern of the area shown in (c) revealing a single set of sixfold symmetry diffraction spots. e) Schematic illustration of MoTe<sub>2</sub> on the nanochip during in situ heating TEM observation at 880 °C for 1 s. f) Low-magnification HR-TEM image of the same area in (b) after a heating pulse at 880 °C. g) Magnified area of the dotted white box in (f). The distinct striped domains of 1T' MoTe<sub>2</sub> can be identified together with the coherent interface between the 2H MoTe<sub>2</sub> and 1T' MoTe<sub>2</sub> domains. h) FFT pattern of the area shown in (g), containing two sets of diffraction spots, one of which belongs to the sixfold symmetric 2H MoTe<sub>2</sub> and the other corresponds to the monoclinic crystal structure of 1T' MoTe<sub>2</sub>.

Owing to the uneven thickness of transferred TMDCs, the phase transitions in TMDCs occur sequentially from thin region to thick region while the complete phase transition is extremely difficult to attain by conventional annealing. Therefore, to accomplish complete phase transition of TMDCs, more complex techniques such as flux-controlled growth must be explored.<sup>[14,24]</sup> Because of the partial phase transition induced by spike thermal annealing, the semimetallic 1T' MoTe<sub>2</sub> is formed and embedded in the semiconducting 2H MoTe<sub>2</sub> and the covalent bond between these two phases leads to the formation of a seamlessly stitched interface shown in Figure S3 in the Supporting Information.<sup>[29,39]</sup> Near the seamless interface, 2H MoTe<sub>2</sub> can be viewed as sandwiches of Te-Mo-Te, in which Mo atoms are coordinated by six Te atoms; while in the phase-transitioned 1T' MoTe<sub>2</sub>, the coordination around Mo atoms are slightly distorted octahedral Te atoms.<sup>[40,41]</sup> The seamless stitched interface formed after phase transition can be depicted as the connection between the pristine Mo-Te bonds and glided Mo-Te bonds.<sup>[3]</sup> With the seamless interface, the 1T' MoTe<sub>2</sub> embedded 2H MoTe<sub>2</sub> can be considered as 1T'-enriched MoTe<sub>2</sub>, whose bandgap can be verified from the semimetallic 1T' MoTe<sub>2</sub> and semiconducting 2H MoTe<sub>2</sub> depending on the phase proportion,<sup>[42]</sup> thus providing an approach for bandgap engineering of MoTe<sub>2</sub>, as demonstrated in the subsequent photodetector application. Furthermore, the seamless connection between the original 2H MoTe<sub>2</sub> and phase transition-induced

1T' MoTe<sub>2</sub> makes a contribution to the exceptional performance of the MoTe<sub>2</sub>-based homojunction device we prepared later.

The detailed hexagonal and monoclinic structures near the boundary are amplified on the atomic scale as shown in Figure 2a,d, respectively. The insets show the FFT patterns. The pattern of 2H MoTe<sub>2</sub> shows a hexagonal symmetry, but that of the formed 1T' MoTe<sub>2</sub> displays a rectangular shape consistent with previous studies.<sup>[24,29]</sup> To exclude the influence of high temperature induced sample drift and elucidate the clear lattice structure of 1T' MoTe<sub>2</sub>, selected-area electron diffraction (SAED) and high-angle annular dark-field detector scanning transmission electron microscopy (HAADF-STEM) are performed on the pristine 2H MoTe<sub>2</sub> and 1T' MoTe<sub>2</sub> materials (supplied by HQ Graphene Co., Ltd.) for comparison, as shown in Figure 2b,e, respectively. The SAED and STEM images obtained from the pristine 2H MoTe<sub>2</sub> validate the existence of the hexagonal lattice structure. Meanwhile, without the sample drift at the high temperature, the results collected from the pristine 1T' MoTe<sub>2</sub> at room temperature are rather distinct and the monoclinic lattice structure is also revealed, which verifies the formation of 1T' MoTe<sub>2</sub> after a spike heating at 880 °C. The simulated STEM images of the ideal 2H MoTe<sub>2</sub> and 1T' MoTe<sub>2</sub> monolayer are shown in the left column in Figure 2c,f, in which the bright spots correspond to Te atoms and Mo atoms are gray spots. The schematic diagrams of 2H MoTe<sub>2</sub> and 1T' MoTe<sub>2</sub> in ball-and-stick presentations are exhibited in the right column

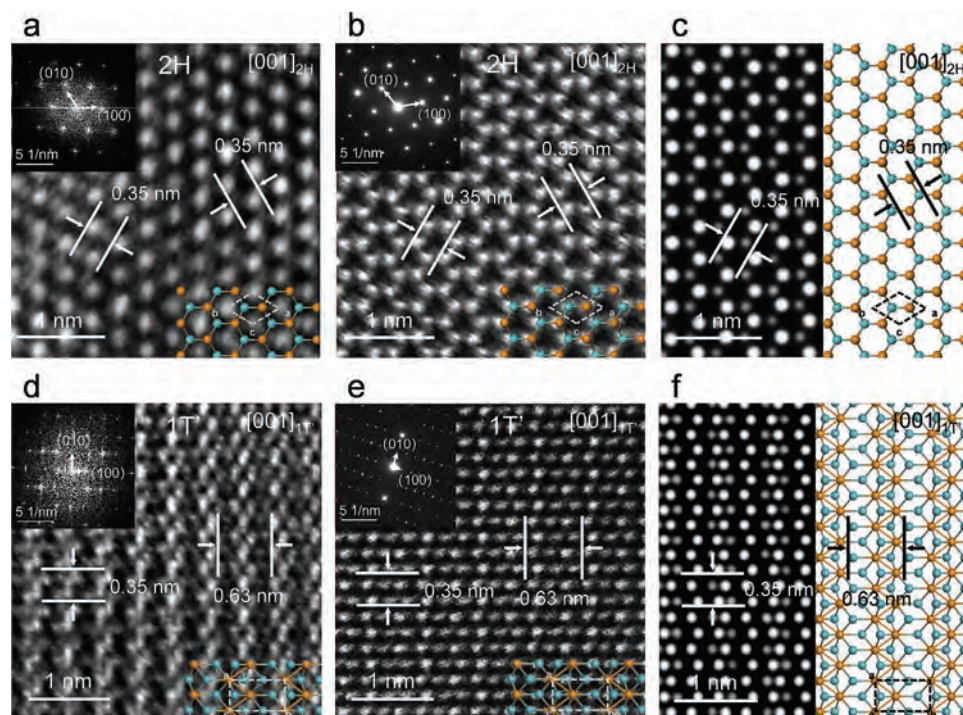


**Figure 2.** HR-TEM and STEM characterizations of 2H MoTe<sub>2</sub> and 1T' MoTe<sub>2</sub> flakes. a,d) High-magnification HR-TEM images and inset FFT patterns of the two areas near the coherent interface in Figure 1g, representing the 2H MoTe<sub>2</sub> and heat-induced 1T' MoTe<sub>2</sub> phase structures, respectively. b,e) HAADF-STEM images and SAED patterns of raw 2H MoTe<sub>2</sub> and raw 1T' MoTe<sub>2</sub> flakes for comparison. c,f) Left column: Simulated HAADF-STEM images of 2H MoTe<sub>2</sub> and 1T' MoTe<sub>2</sub> lattices; Right column: Schematic diagrams of 2H MoTe<sub>2</sub> and 1T' MoTe<sub>2</sub> in ball-and-stick presentations (orange spheres are Mo atoms and blue spheres are Te atoms).

of Figure 2c,f. The black dashed boxes represent the primitive unit cells and a distinct atomic lattice symmetry between the hexagonal and monoclinic cells is shown. Both the TEM and STEM images obtained from 2H MoTe<sub>2</sub> and 1T' MoTe<sub>2</sub> (pristine or heat-induced) agree with the simulated STEM images.

## 2.2. MoTe<sub>2</sub>-Based Lateral Homo Junction Field-Effect Transistor

Band alignment engineering is booming to improve the charge transfer efficiency of TMDCs-based heterostructures for functional devices such as photodetector.<sup>[43–45]</sup> Besides, regardless of lattice mismatch, homo junction is another kind of promising structure in TMDCs-based FETs.<sup>[20]</sup> On account of the small barrier difference between 2H MoTe<sub>2</sub> ( $\approx 1$  eV) and 1T' MoTe<sub>2</sub> ( $\approx 60$  meV),<sup>[6]</sup> the lateral 2H/1T' homo junction MoTe<sub>2</sub> FET is expected to provide fast carrier separation and charge transfer properties as reported previously.<sup>[23,28]</sup> Laser-induced phase patterning has been proposed to construct the 1T'/2H MoTe<sub>2</sub> homo junction which originates from Te vacancies in the desired region driven by local heating.<sup>[1,46]</sup> The generated Te vacancies are not the atomic defects that affect the device performance, but act as an inducement for phase transition. In our study, the successful phase transition is simply achieved by the control of Te sublimation assisted by the impermeable properties of h-BN.<sup>[1]</sup> As schematically demonstrated in **Figure 3a**, the exposed 2H MoTe<sub>2</sub> starts the structural phase transition from 2H to 1T' after thermal annealing at 880 °C under an Ar/H<sub>2</sub> atmosphere to form the 1T'-enriched phase

region, whereas the 2H phase remains intact in the desired region covered by the thick h-BN flake (detailed information provided in Experimental Section and Figures S4 and S5, Supporting Information). The optical contrast between the 2H and 1T'-enriched regions is rather distinct as shown in **Figure 3b**. Formation of the 1T'-enriched MoTe<sub>2</sub>/2H MoTe<sub>2</sub> homo junction is verified by Raman line mapping as shown in **Figure 3c**. In the case of the h-BN encapsulated 2H MoTe<sub>2</sub>, the Raman scattering spectra exhibit the typical E<sub>2g</sub> ( $\approx 233$  cm<sup>-1</sup>) (“in-plane” vibrational mode) and A<sub>1g</sub> ( $\approx 171$  cm<sup>-1</sup>) (“out-of-plane” vibrational mode) peaks, which are the same as those of the pristine 2H MoTe<sub>2</sub>.<sup>[24,47]</sup> In the exposed MoTe<sub>2</sub> area, the new peaks of A<sub>g</sub> ( $\approx 79$ ,  $\approx 139$ , and  $\approx 249$  cm<sup>-1</sup>), A<sub>u</sub> ( $\approx 110$  cm<sup>-1</sup>) and B<sub>g</sub> ( $\approx 163$  cm<sup>-1</sup>) suggest the local phase transition from 2H to 1T'.<sup>[1,6,14,17,23,29]</sup> The remaining E<sub>2g</sub> peak with attenuated intensity indicates the formation of mixed-phase MoTe<sub>2</sub> and it is dominated by the 1T' phase according to the Raman peak intensity comparison.<sup>[48,49]</sup> In addition, the weak A<sub>1g</sub> peak associated with 2H MoTe<sub>2</sub> could be further attenuated and submerged by B<sub>g</sub> peak corresponding to the newly formed 1T' MoTe<sub>2</sub>. The Raman results imply that coverage of thick h-BN limits sublimation of Te atoms even at a high temperature thereby preventing the phase transition from 2H to 1T' in MoTe<sub>2</sub>.

By means of the impermeable h-BN, the phase transition from 2H to 1T' phase in MoTe<sub>2</sub> can be modulated locally, and the 1T'-enriched MoTe<sub>2</sub>/2H MoTe<sub>2</sub> homo junction FET is constructed. In order to investigate the electrical difference between 2H MoTe<sub>2</sub> and the 1T'-enriched MoTe<sub>2</sub>, the transport characteristics of the transistors built on pure 2H MoTe<sub>2</sub>

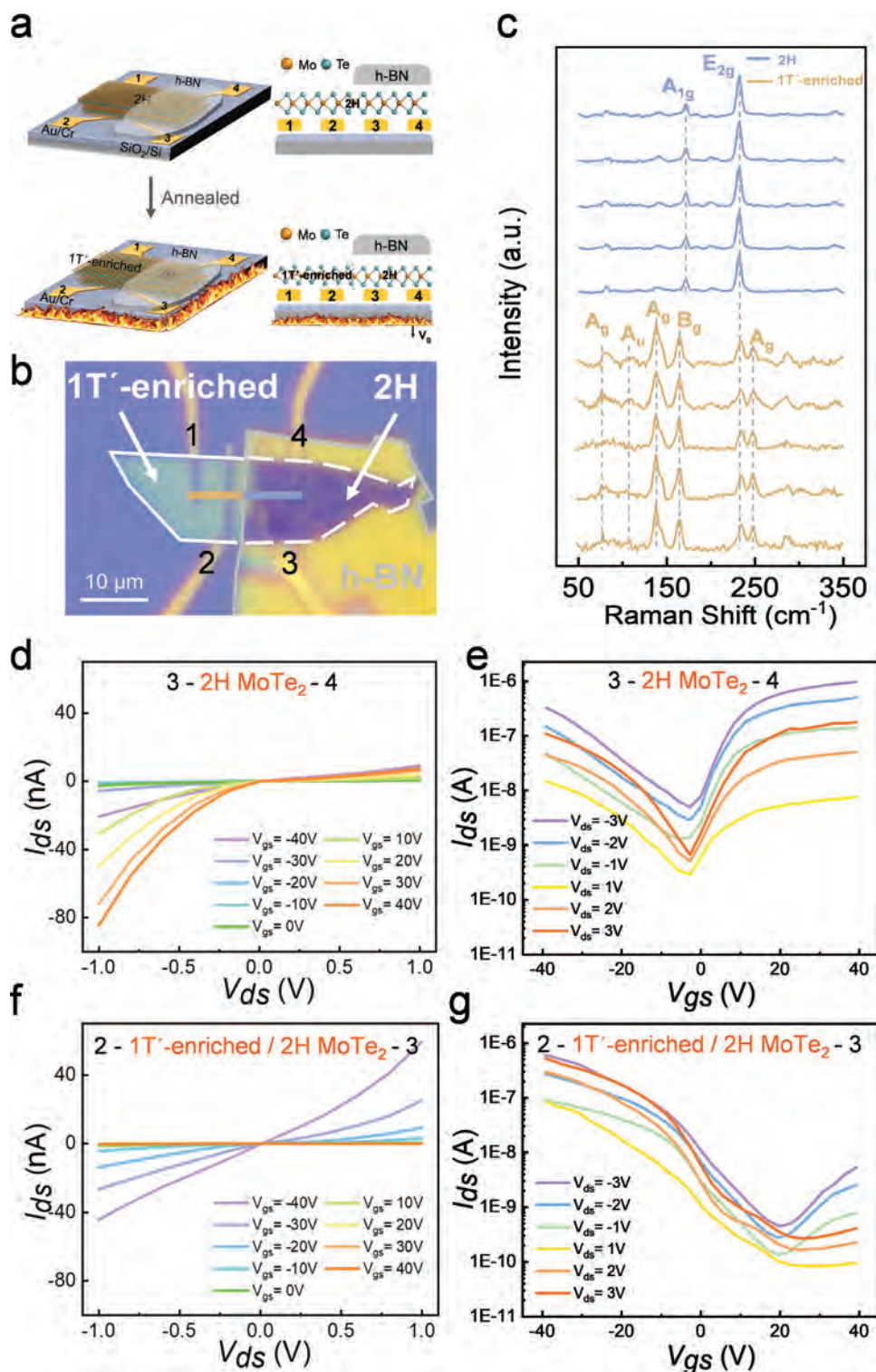


**Figure 3.** Verification of the heat-induced phase transition in 2H MoTe<sub>2</sub> and electrical characteristics of the lateral MoTe<sub>2</sub> homojunction. a) Schematic illustration (planar and cross-section) of the homojunction device fabricated by the heat-induced phase transition process. b) Optical image of the lateral 1T'-enriched MoTe<sub>2</sub>/2H MoTe<sub>2</sub> homojunction half-covered by h-BN. c) Raman line mapping collected along the lateral 1T'-enriched MoTe<sub>2</sub>/2H MoTe<sub>2</sub> homojunction device. d,f) Output characteristics of the two devices with the pure 2H MoTe<sub>2</sub> channel and lateral 1T'-enriched MoTe<sub>2</sub>/2H MoTe<sub>2</sub> homojunction. e) Semilog transfer characteristics of the device with the pure 2H MoTe<sub>2</sub> channel showing the behavior of an ambipolar FET with CNPs at  $V_{gs} = 0$  V. g) Semilog transfer characteristics of the device with the 1T'-enriched MoTe<sub>2</sub>/2H MoTe<sub>2</sub> homojunction showing the behavior of a p-type transistor with CNPs at  $V_{gs} = 20$  V.

(between electrode 3 and 4, as marked in Figure 3b) and 1T'-enriched MoTe<sub>2</sub>/2H MoTe<sub>2</sub> homojunction (between electrode 2 and 3) are compared in Figure 3d–g. Back gate voltage ( $V_g$ ) is applied through *n*-Si substrate, upon which 300 nm SiO<sub>2</sub> is grown by thermal oxidation. After the preparation of four bottom electrodes (as the number marked in Figure 3a), the 1T'-enriched MoTe<sub>2</sub>/2H MoTe<sub>2</sub> homojunction is prepared above the electrode with the help of h-BN by one-step annealing as mentioned above. With regard to the FET with pure 2H MoTe<sub>2</sub> channel (between electrode 3 and 4), the output characteristics in Figure 3d show the typical gate-tunable FET properties. The undesired asymmetric current may be caused by the poor contact between the bottom electrodes and channel materials, thus forming uneven Schottky barriers between electrode 3, 4 and 2H MoTe<sub>2</sub> interface. The transfer characteristics at room temperature (Semilog  $I_{ds} - V_{gs}$ ) in Figure 3e display the ambipolar conductive behavior due to the formation of Schottky barriers at the interface between electrode and 2H MoTe<sub>2</sub>.<sup>[9,50]</sup> In contrast to the transistor with pure 2H MoTe<sub>2</sub> channel, the FET based on the 1T'-enriched MoTe<sub>2</sub>/2H MoTe<sub>2</sub> homojunction channel (between electrode 2 and 3) shows larger drain-to-source currents at a negative  $V_{gs}$  (Figure 3d,f). It can be attributed to the formation of 1T'-enriched MoTe<sub>2</sub> region, whose bandgap is assumed to vary between those of the semimetallic 1T' MoTe<sub>2</sub> and semiconducting 2H MoTe<sub>2</sub>.<sup>[42]</sup> Therefore, compared to the large Schottky barrier between the metal electrodes and 2H MoTe<sub>2</sub>, in which the carriers are retarded by the sharp junction forming at the metal electrodes/2H MoTe<sub>2</sub> interface, formation of the 1T'-enriched MoTe<sub>2</sub> is conducive to changing the abrupt bandgap to the gradient bandgap.<sup>[51,52]</sup> Thus, a lower contact resistance between the electrode and homojunction channel has formed, resulting in the ohmic contact (as the linear  $I$ - $V$  curve shown in Figure 3f). Such a gradient bandgap formed among metal/1T'-enriched MoTe<sub>2</sub>/2H MoTe<sub>2</sub> may assist to extend the carrier lifetime, boost the carrier transfer, and reduce the charge recombination rate consequently improving the performance of the FET comprising the 1T'-enriched MoTe<sub>2</sub>/2H MoTe<sub>2</sub> homojunction channel.<sup>[53]</sup> The transfer characteristics of the 1T'-enriched MoTe<sub>2</sub>/2H MoTe<sub>2</sub> homojunction in Figure 3g indicate p-type conduction with an ON/OFF current ratio of  $1.32 \times 10^3$  ( $V_{ds} = -3$  V). The values of  $V_{gs}$  at the minimum drain-source current ( $I_{ds}$ ) are defined as the charge neutrality points (CNPs) and shift from  $\approx 0$  V (Figure 3e) to  $\approx 20$  V (Figure 3g), indicating p-doping effects after the phase transition.<sup>[54]</sup> Previous studies have shown that fabrication of MoTe<sub>2</sub> FETs by rapid thermal annealing also results in p-doping, which attributes to the absorbed molecules form air or tellurium defects derived from phase transition.<sup>[55–57]</sup> Furthermore, the doping effects produce low  $I_{ds}$  at a positive  $V_{gs}$  (Figure 3f) due to neutralization of hole carriers and doped electrons.

### 2.3. MoTe<sub>2</sub>-Based Lateral Homojunction Optoelectronic Devices

Figure 4a shows the schematic illustration of the lateral homojunction illuminated with a 520 nm laser (gate bias of 0 V). By applying laser irradiation to the center between different electrodes, the photocurrents of the MoTe<sub>2</sub>-based photodetector devices can be measured. The output curves in Figure 4b,c

illustrate that the transistors with pure 2H MoTe<sub>2</sub> (between electrode 3 and 4) and the 1T'-enriched MoTe<sub>2</sub>/2H MoTe<sub>2</sub> (between electrode 2 and 3) homojunction under laser illumination with different incident power, respectively. It is found that the 1T'-enriched MoTe<sub>2</sub>/2H MoTe<sub>2</sub> homojunction shows a considerable photocurrent increment, which is approximately ten times larger than that of the transistor with the pure 2H MoTe<sub>2</sub> channel. The increase in photocurrent is believed to be caused by the formation of the 1T'-enriched MoTe<sub>2</sub>/2H MoTe<sub>2</sub> homojunction after annealing, and the MoTe<sub>2</sub>-based homojunction creates a built-in electric field during exposure to light as conventional heterojunction.<sup>[58,59]</sup> Upon light illumination, electron-hole pairs are separated to produce a large drain-to-source current (Figure 4c).<sup>[60,61]</sup> The time-resolved dynamic photoresponse of the devices under 520 nm light illumination of various incident powers at  $V_{ds} = 0$  V is shown in Figure 4e,f. The homojunction device has superior sensitivity and stability compared to the device with the pure 2H MoTe<sub>2</sub> channel. The photoresponsivity ( $R$ ) and detectivity ( $D^*$ ) can be calculated by  $R = I_{\text{photocurrent}}/PA$ ,  $D^* = R/(2qI_{\text{dark}}/A)^{1/2}$ , respectively, in which  $P$  is the power of the incident light,  $A$  is the effective power illumination area, and  $q$  is the elementary charge.<sup>[62,63]</sup> An increase of 36 nA in  $I_{ds}$  is observed for light power of 200  $\mu$ W and the calculated photoresponsivity and detectivity are  $\approx 2.8 \times 10^{-4}$  A W<sup>-1</sup> and  $\approx 2.8 \times 10^9$  Jones (the  $P$  and  $A$  here are reckoned as  $4 \times 10^{-3}$  mW cm<sup>-2</sup> and 32  $\mu$ m<sup>2</sup>), respectively. The rise time (defined as the time taken by the photocurrent to rise from 10% to 90% of the final value) and fall time (similarly defined as the time taken by the photocurrent to fall from 90% to 10% of the final value) of the photocurrent at a zero bias under high-frequency illumination (400 Hz, 1 mW) are 384 and 473  $\mu$ s, respectively, as shown in Figure 4d. The photoresponse of the 1T'-enriched MoTe<sub>2</sub>/2H MoTe<sub>2</sub> homojunction is considerably faster than that of the other MoTe<sub>2</sub>-based photodetectors reported previously (the related devices and their performance are listed in Supporting Section 6, Supporting Information), in which the relatively longer response time is related to materials defects.<sup>[64]</sup>

It is well known that the hexagonal 2H MoTe<sub>2</sub> is semiconducting with the bandgap of  $\approx 1$  eV, while 1T' MoTe<sub>2</sub> is typically semimetallic with the bandgap of  $\approx 60$  meV. Therefore, the bandgap of 1T'-enriched MoTe<sub>2</sub> should vary between 1T' MoTe<sub>2</sub> and 2H MoTe<sub>2</sub> depending on the amount of 1T' MoTe<sub>2</sub>.<sup>[35]</sup> The seamless stitching of 1T'-enriched MoTe<sub>2</sub> and 2H MoTe<sub>2</sub> provides an effective approach to realize the gradient bandgap in MoTe<sub>2</sub>. Compared to abrupt bandgap, the gradient bandgap has smoother structure in which electrons can transport directly between the electrode and channel material due to effective funneling.<sup>[65,66]</sup> In our study, we believe that the gradient bandgap alignment in 1T'-enriched MoTe<sub>2</sub>/2H MoTe<sub>2</sub> lateral homojunction is responsible for the high-speed channel for charge separation and carrier transportation, resulting in the fast photoresponse.<sup>[52]</sup> Similar bandgap modulation strategies have been adopted to improve the performances of different devices. For example, Jia et al. have fabricated perovskite nanoplatelets with a gradient bandgap (2.29–1.56 eV) and the effective funneling can boost carrier diffusion.<sup>[65]</sup> Zhuang et al. have developed a bandgap graded CdS<sub>*x*</sub>Se<sub>1-*x*</sub> nanowire waveguide with the superior ability in driving carrier transportation.<sup>[21]</sup> Lan

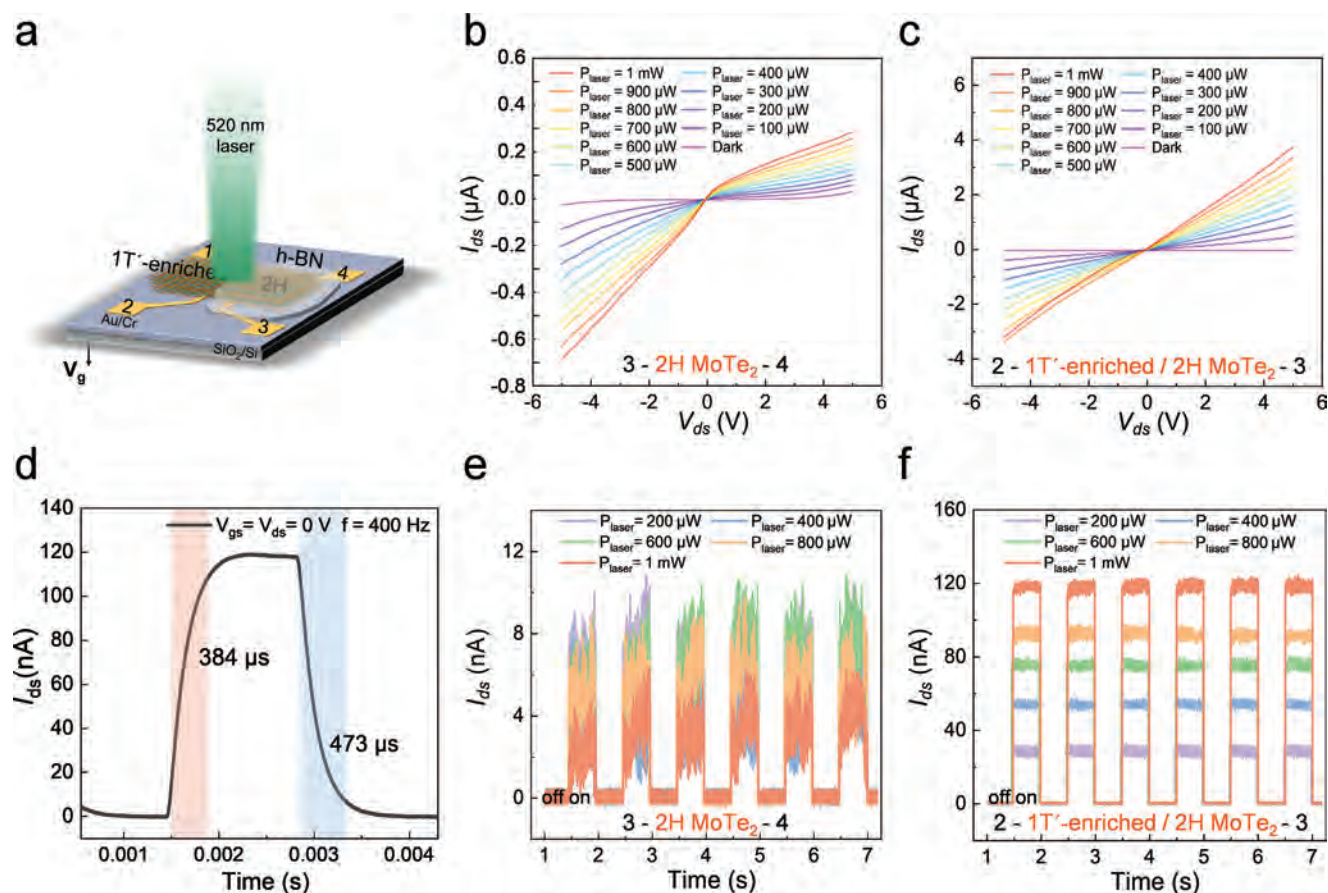


**Figure 4.** Photoresponse of the MoTe<sub>2</sub> homojunction photodetector. a) Schematic illustration of the lateral 1T'-enriched MoTe<sub>2</sub>/2H MoTe<sub>2</sub> homojunction photodetector illuminated by a 520 nm laser. b,c) Photocurrents of two photodetectors with the pure 2H MoTe<sub>2</sub> channel and lateral 1T'-enriched MoTe<sub>2</sub>/2H MoTe<sub>2</sub> homojunction versus bias voltages for different laser power. d) Response and recovery cycle for the rise/fall time analysis of the photodetector built on the lateral 1T'-enriched MoTe<sub>2</sub>/2H MoTe<sub>2</sub> homojunction. e,f) Dynamic photoresponse curves of two photodetectors with the pure 2H MoTe<sub>2</sub> channel and lateral 1T'-enriched MoTe<sub>2</sub>/2H MoTe<sub>2</sub> homojunction for different laser power at V<sub>ds</sub> = 0 V.

et al. have fabricated a photodetector with stacked multilayer graphene oxide nanoribbons and the gradually varying bandgap leads to a fast response time.<sup>[22]</sup> Therefore, the construction of gradient bandgap has significant application in improving the performance of optoelectronic devices, which needs to be explored with the detailed calculation or further experiments in the future.

### 3. Conclusion

In summary, the local phase transition from semiconducting 2H MoTe<sub>2</sub> to semimetallic 1T' MoTe<sub>2</sub> is monitored by in situ heating TEM observation, changes in atomic structure from 2H MoTe<sub>2</sub> to 1T' MoTe<sub>2</sub> are presented, and the seamless connection between these two phases are demonstrated, which has contributed to the magnificent electric properties in the 1T'-enriched MoTe<sub>2</sub>/2H MoTe<sub>2</sub> homojunction FET. By controlling the mixed phase in the desired area via patterning h-BN on MoTe<sub>2</sub>, a photodetector with the lateral 1T'-enriched MoTe<sub>2</sub>/2H MoTe<sub>2</sub> homojunction is fabricated. Compared to the pure 2H MoTe<sub>2</sub> photodetector, the device consisting of the 1T'-enriched MoTe<sub>2</sub>/2H MoTe<sub>2</sub> homojunction exhibits fast

photo response and ten times larger photocurrents due to gradient bandgap alignment. The phase transition in MoTe<sub>2</sub> provides insights into phase engineering of other TMDCs and this promising approach has large potential in fabricating high performance homojunction optoelectronic and electronic devices.

### 4. Experimental Section

**TEM/STEM Characterization:** The bulk 2H MoTe<sub>2</sub> and 1T' MoTe<sub>2</sub> supplied by HQ Graphene Co., Ltd. were pulverized mechanically into small pieces in the glove box to avoid contact with oxygen and vapor.<sup>[67,68]</sup> Figure S1 in the Supporting Information shows the magnified optical image of the heating nanochip supplied by Wildfire, Dens solution Co., Ltd. For in situ heating TEM examination, the 2H MoTe<sub>2</sub> debris were mixed evenly, sonicated in ethanol, and then put on the transparent windows of the nanochip under an optical microscope. After evaporation of ethanol, the 2H MoTe<sub>2</sub> fragments were observed at 80 kV by TEM (aberration-corrected JEM-ARM300F) with a heating holder. The heating program was designed to reach the target temperature at a high rate of 290 °C s<sup>-1</sup>, then proceeded the annealing process for 1 s (Figure S2a, Supporting Information). In the STEM examination, the 2H MoTe<sub>2</sub> and 1T' MoTe<sub>2</sub> samples were prepared as described above but copper grids were used instead of nanochips to hold the samples.

**Device Fabrication and Characterization:** Prior to device fabrication, four parallel electrodes were defined by electron beam lithography (Zeiss Sigma system) and Cr/Au (5/40 nm) was deposited by electron beam evaporation (Kurt J. Lesker system) to avoid influence of polymethyl methacrylate and the electron beam on the electron transport properties of MoTe<sub>2</sub>.<sup>[48,51]</sup> 2H MoTe<sub>2</sub> and thick h-BN flakes were exfoliated mechanically and dry transferred onto the prepared electrodes on SiO<sub>2</sub>/Si substrate using PF gel films (Gel Pak Co., Ltd.) successively. After annealing at the optimal temperature of 880 °C, the exposed 2H MoTe<sub>2</sub> evolved into the 1T'-enriched phase whereas the 2H phase remains intact at the h-BN covered area, leading to the formation of the lateral 1T'-enriched MoTe<sub>2</sub>/2H MoTe<sub>2</sub> homojunction. The annealing temperature was the same as that in situ TEM measurement at 880 °C, but a longer annealing time was adopted for the improved heat dissipation of the SiO<sub>2</sub>/Si substrate.<sup>[39]</sup> The morphology of the homojunction device was examined by atomic force microscopy (Bruker Multimode 8) using the tapping mode and Raman scattering (HORIBA Jobin Yvon HR800) was performed to monitor the characteristic peaks using a 514 nm excitation laser (details provided in Supporting Section 4, Supporting Information). The electrical and optoelectronic measurements were performed under ambient conditions at room temperature using the commercial high-resolution photoelectric scanning technique (MStarter 200). In the photocurrent measurements, the laser was focused through a 50 × objective lens to produce a spot size of about 8 μm.

## Supporting Information

Supporting Information is available from the Wiley Online Library or from the author.

## Acknowledgements

This work was supported by National Natural Science Foundation of China (Grant Nos. 51925208 and 61974157), Key Research Project of Frontier Science, Chinese Academy of Sciences (QYZDB-SSW-JSC021), Science and Technology Innovation Action Plan of Shanghai Science and Technology Committee (20501130700), Key Research Program of the Chinese Academy of Sciences (XDPB22), Strategic Priority Research Program (B) of the Chinese Academy of Sciences (XDB30030000), Science and Technology Commission of Shanghai Municipality (21JC1406100 and 19JC1415500), and City University of Hong Kong Strategic Research Grant (SRG 7005505).

## Conflict of Interest

The authors declare no conflict of interest.

## Data Availability Statement

The data that support the findings of this study are available on request from the corresponding author. The data are not publicly available due to privacy or ethical restrictions.

## Keywords

gradient bandgaps, homojunctions, in situ transmission electron microscopy (TEM), MoTe<sub>2</sub>, phase transitions

Received: February 11, 2022  
Revised: March 26, 2022  
Published online: April 11, 2022

- [1] S. Cho, S. Kim, J. H. Kim, J. Zhao, J. Seok, D. H. Keum, J. Baik, D. H. Choe, K. J. Chang, K. Suenaga, S. W. Kim, Y. H. Lee, H. Yang, *Science* **2015**, *349*, 625.
- [2] A. N. Enyashin, L. Yadgarov, L. Houben, I. Popov, M. Weidenbach, R. Tenne, M. Bar-Sadan, G. Seifert, *J. Phys. Chem. C* **2011**, *115*, 24586.
- [3] A. V. Kolobov, P. Fons, J. Tominaga, *Phys. Rev. B* **2016**, *94*, 094114.
- [4] R. Kappera, D. Voiry, S. E. Yalcin, B. Branch, G. Gupta, A. D. Mohite, M. Chhowalla, *Nat. Mater.* **2014**, *13*, 1128.
- [5] A. Ambrosi, Z. Sofer, M. Pumera, *Chem. Commun.* **2015**, *51*, 8450.
- [6] D. H. Keum, S. Cho, J. H. Kim, D. H. Choe, H. J. Sung, M. Kan, H. Kang, J. Y. Hwang, S. W. Kim, H. Yang, K. J. Chang, Y. H. Lee, *Nat. Phys.* **2015**, *11*, 482.
- [7] K. Deng, G. L. Wan, P. Deng, K. N. Zhang, S. J. Ding, E. Y. Wang, M. Z. Yan, H. Q. Huang, H. Y. Zhang, Z. L. Xu, J. Denlinger, A. Fedorov, H. T. Yang, W. H. Duan, H. Yao, Y. Wu, S. S. Fan, H. J. Zhang, X. Chen, S. Y. Zhou, *Nat. Phys.* **2016**, *12*, 1105.
- [8] Z. J. Xie, W. Y. Lei, W. F. Zhang, Y. Liu, L. Yang, X. K. Wen, H. X. Chang, *Adv. Mater. Interfaces* **2021**, *8*, 2002023.
- [9] F. Zhang, H. R. Zhang, S. Krylyuk, C. A. Milligan, Y. Q. Zhu, D. Y. Zemlyanov, L. A. Bendersky, B. P. Burton, A. V. Davydov, J. Appenzeller, *Nat. Mater.* **2019**, *18*, 55.
- [10] P. L. Li, J. Cui, J. D. Zhou, D. Guo, Z. Z. Zhao, J. Yi, J. Fan, Z. Q. Ji, X. N. Jing, F. M. Qu, C. L. Yang, L. Lu, J. H. Lin, Z. Liu, G. T. Liu, *Adv. Mater.* **2019**, *31*, 1904641.
- [11] Y. C. Lin, D. O. Dumcencu, Y. S. Huang, K. Suenaga, *Nat. Nanotechnol.* **2014**, *9*, 391.
- [12] C. Ghosh, M. K. Singh, S. Parida, M. T. Janish, A. Doble, A. M. Dongare, C. B. Carter, *Sci. Rep.* **2021**, *11*, 9014.
- [13] P. Gao, L. P. Wang, Y. Y. Zhang, Y. Huang, K. H. Liu, *ACS Nano* **2015**, *9*, 11296.
- [14] X. K. Zhu, A. L. Li, D. Wu, P. Zhu, H. Y. Xiang, S. Liu, J. Sun, F. P. Ouyang, Y. Zhou, X. Xiong, *J. Mater. Chem. C* **2019**, *7*, 10598.
- [15] L. Yang, H. Wu, W. F. Zhang, Z. H. Chen, J. Li, X. Lou, Z. J. Xie, R. Zhu, H. X. Chang, *Nanoscale* **2018**, *10*, 19906.
- [16] H. Zhu, Q. X. Wang, L. X. Cheng, R. Addou, J. Y. Kim, M. J. Kim, R. M. Wallace, *ACS Nano* **2017**, *11*, 11005.
- [17] S. Song, D. H. Keum, S. Cho, D. Perello, Y. Kim, Y. H. Lee, *Nano Lett.* **2016**, *16*, 188.
- [18] M. Ran, X. Xu, X. Kong, Y. H. Lee, W. J. Cui, Z. -Y. Hu, R. Alexander, Z. T. Luo, H. Q. Li, F. Ding, L. Gan, T. Y. Zhai, *Fundam. Res.* **2022**, <https://doi.org/10.1016/j.fmre.2021.11.020>.
- [19] P. Wang, Y. Yang, E. Pan, F. C. Liu, P. M. Ajayan, J. D. Zhou, Z. Liu, *Small* **2021**, *18*, 2105215.
- [20] F. K. Wang, K. Pei, Y. Li, H. Q. Li, T. Y. Zhai, *Adv. Mater.* **2021**, *33*, 2005303.
- [21] P. Fan, H. W. Liu, X. J. Zhuang, W. H. Zheng, C. H. Ge, W. Huang, X. Yang, Y. Liu, Y. Jiang, X. L. Zhu, A. L. Pan, *Nanoscale* **2019**, *11*, 8494.
- [22] Y. W. Lan, C. M. Torres, X. D. Zhu, C. L. Sun, S. L. Zhu, C. D. Chen, K. L. Wang, *Nano Energy* **2016**, *27*, 114.
- [23] D. L. Lu, Z. Q. Li, C. S. Xu, S. W. Luo, C. Y. He, J. Li, G. Guo, G. L. Hao, X. Qi, J. X. Zhong, *Nano Res.* **2021**, *14*, 1311.
- [24] J. C. Park, S. J. Yun, H. Kim, J. H. Park, S. H. Chae, S. J. An, J. G. Kim, S. M. Kim, K. K. Kim, Y. H. Lee, *ACS Nano* **2015**, *9*, 6548.
- [25] H. C. Diaz, Y. J. Ma, R. Chaghi, M. Batzill, *Appl. Phys. Lett.* **2016**, *108*, 191606.
- [26] P. Kumar, J. P. Horwath, A. C. Foucher, C. C. Price, N. Acero, V. B. Shenoy, E. A. Stach, D. Jariwala, *NPJ 2D Mater. Appl.* **2020**, *4*, 16.
- [27] W. Y. Chen, Z. Wang, K. V. Bets, D. X. Luong, M. Q. Ren, M. G. Stanford, E. A. McHugh, W. A. Algozeeb, H. Guo, G. H. Gao, B. Deng, J. H. Chen, J. T. Li, W. T. Carsten, B. I. Yakobson, J. M. Tour, *ACS Nano* **2021**, *15*, 1282.



- [28] R. Ma, H. R. Zhang, Y. Yoo, Z. P. Degregorio, L. Jin, P. Golani, J. G. Azadani, T. Low, J. E. Johns, L. A. Bendersky, A. V. Davydov, S. J. Koester, *ACS Nano* **2019**, *13*, 8035.
- [29] Q. Zhang, X. F. Wang, S. H. Shen, Q. Lu, X. Z. Liu, H. Y. Li, J. Y. Zheng, C. P. Yu, X. Y. Zhong, L. Gu, T. L. Ren, L. Y. Jiao, *Nat. Electron.* **2019**, *2*, 164.
- [30] X. J. Wang, J. Shang, M. J. Zhu, X. Zhou, R. Hao, L. N. Sun, H. Xu, J. B. Zheng, X. F. Lei, C. Li, L. Z. Kou, Q. L. Feng, *Nanoscale Horiz.* **2020**, *5*, 954.
- [31] K. A. N. Duerloo, Y. Li, E. J. Reed, *Nat. Commun.* **2014**, *5*, 4214.
- [32] Z. W. Wang, X. Y. Li, G. Z. Zhang, Y. Luo, J. Jiang, *ACS Appl. Mater. Interfaces* **2017**, *9*, 23309.
- [33] S. Kang, D. Won, H. Yang, C. H. Lin, C. S. Ku, C. Y. Chiang, S. Kim, S. Cho, *Appl. Surf. Sci.* **2021**, *563*, 150282.
- [34] C. Si, D. Choe, W. Y. Xie, H. Wang, Z. M. Sun, J. Bang, S. B. Zhang, *Nano Lett.* **2019**, *19*, 3612.
- [35] Y. Tan, F. Luo, M. J. Zhu, X. L. Xu, Y. Ye, B. Li, G. Wang, W. Luo, X. M. Zheng, N. N. Wu, Y. Y. Yu, S. Q. Qin, X. A. Zhang, *Nanoscale* **2018**, *10*, 19964.
- [36] Q. Tang, *J. Mater. Chem. C* **2018**, *6*, 9561.
- [37] J. H. Lin, S. T. Pantelides, W. Zhou, *ACS Nano* **2015**, *9*, 5189.
- [38] X. Lin, J. C. Lu, Y. Shao, Y. Y. Zhang, X. Wu, J. B. Pan, L. Gao, S. Y. Zhu, K. Qian, Y. F. Zhang, D. L. Bao, L. F. Li, Y. Q. Wang, Z. L. Liu, J. T. Sun, T. Lei, C. Liu, J. O. Wang, K. Ibrahim, D. N. Leonard, W. Zhou, H. M. Guo, Y. L. Wang, S. X. Du, S. T. Pantelides, H. J. Gao, *Nat. Mater.* **2017**, *16*, 717.
- [39] X. L. Xu, B. Han, S. Liu, S. Q. Yang, X. H. Jia, W. J. Xu, P. Gao, Y. Ye, L. Dai, *Adv. Mater.* **2020**, *32*, 2000236.
- [40] W. G. Dawson, D. W. Bullett, *J. Phys.* **1987**, *20*, 6159.
- [41] Y. Wang, J. Xiao, H. Y. Zhu, Y. Li, Y. Alsaied, K. Y. Fong, Y. Zhou, S. Q. Wang, W. Shi, Y. Wang, A. Zettl, E. J. Reed, X. Zhang, *Nature* **2017**, *550*, 487.
- [42] R. C. Xie, M. Hu, D. Q. Liu, Y. Y. Yu, C. Li, J. He, J. Luo, *Appl. Phys. Lett.* **2020**, *117*, 163103.
- [43] R. Liu, F. K. Wang, L. X. Liu, X. Y. He, J. Z. Chen, Y. Li, T. Y. Zhai, *Small Struct.* **2021**, *2*, 2000136.
- [44] J. Y. Tan, S. S. Li, B. L. Liu, H. M. Cheng, *Small Struct.* **2021**, *2*, 2000093.
- [45] F. K. Wang, P. Luo, Y. Zhang, Y. Huang, Q. F. Zhang, Y. Li, T. Y. Zhai, *Sci. China Mater.* **2020**, *63*, 1537.
- [46] Z. R. Chen, H. Y. Nan, Z. Liu, X. Y. Wang, X. F. Gu, S. Q. Xiao, *J. Raman Spectrosc.* **2019**, *50*, 755.
- [47] C. Ruppert, O. B. Aslan, T. F. Heinz, *Nano Lett.* **2014**, *14*, 6231.
- [48] T. Kim, H. Park, D. Joung, D. Kim, R. Lee, C. H. Shin, M. Diware, W. Chegal, S. H. Jeong, J. C. Shin, J. Park, S. W. Kang, *Adv. Mater. Interfaces* **2018**, *5*, 1800439.
- [49] H. Kim, J. E. Johns, Y. Yoo, *Small* **2020**, *16*, 2002849.
- [50] Y. F. Lin, Y. Xu, S. T. Wang, S. L. Li, M. Yamamoto, A. Aparecido-Ferreira, W. W. Li, H. B. Sun, S. Nakaharai, W. B. Jian, K. Ueno, K. Tsukagoshi, *Adv. Mater.* **2014**, *26*, 3263.
- [51] G. L. Zhao, H. Kozuka, H. Lin, M. Takahashi, T. Yoko, *Thin Solid Films* **1999**, *340*, 125.
- [52] J. F. Yuan, C. H. Bi, J. H. Xi, R. Q. Guo, J. J. Tian, *J. Phys. Chem. Lett.* **2021**, *12*, 1018.
- [53] H. J. Sun, C. Neumann, T. Zhang, M. Löffler, A. Wolf, Y. Hou, A. Turchanin, J. Zhang, X. L. Feng, *Adv. Mater.* **2019**, *31*, 1900961.
- [54] T. Y. Luo, B. J. Pan, K. N. Zhang, Y. Q. Dong, C. Zou, Z. Y. Gu, L. J. Zhang, *Appl. Surf. Sci.* **2021**, *540*, 148276.
- [55] Y. M. Chang, S. H. Yang, C. Y. Lin, C. H. Chen, C. H. Lien, W. B. Jian, K. Ueno, Y. W. Suen, K. Tsukagoshi, Y. F. Lin, *Adv. Mater.* **2018**, *30*, 1706995.
- [56] Y. Zhou, E. J. Reed, *J. Phys. Chem. C* **2015**, *119*, 21674.
- [57] Y. J. Park, A. K. Katiyar, A. T. Hoang, J. H. Ahn, *Small* **2019**, *15*, 1901772.
- [58] E. X. Wu, Y. Xie, S. J. Wang, D. H. Zhang, X. D. Hu, J. Liu, *Nano Res.* **2020**, *13*, 3445.
- [59] A. Pezeshki, S. Hossein, H. Shokouh, T. Nazari, K. Oh, S. Im, *Adv. Mater.* **2016**, *28*, 3216.
- [60] S. Q. Hu, J. P. Xu, Q. H. Zhao, X. G. Luo, X. T. Zhang, T. Wang, W. Q. Jie, Y. C. Cheng, R. Frisenda, A. Castellanos-Gomez, X. T. Gan, *Adv. Opt. Mater.* **2021**, *9*, 2001802.
- [61] J. Chen, Y. Shan, Q. Wang, J. Zhu, R. Liu, *Nanotechnology* **2020**, *31*, 295201.
- [62] G. Wang, M. Zhang, D. Chen, Q. L. Guo, X. F. Feng, T. C. Niu, X. S. Liu, A. Li, J. W. Lai, D. Sun, Z. M. Liao, Y. Q. Wang, P. K. Chu, G. Q. Ding, X. M. Xie, Z. F. Di, X. Wang, *Nat. Commun.* **2018**, *9*, 5168.
- [63] W. J. Chen, R. R. Liang, S. Q. Zhang, Y. Liu, W. J. Cheng, C. H. Sun, J. Xu, *Nano Res.* **2020**, *13*, 127.
- [64] Y. W. Zhang, K. K. Ma, C. Zhao, W. Hong, C. J. Nie, Z. J. Qiu, S. Wang, *ACS Nano* **2021**, *15*, 4405.
- [65] C. H. Zhou, Q. D. Ou, W. J. Chen, Z. X. Gan, J. Wang, Q. L. Bao, X. M. Wen, B. H. Jia, *Adv. Opt. Mater.* **2018**, *6*, 1801107.
- [66] W. Y. Shao, Y. Li, X. Wang, X. Ouyang, J. F. Cai, C. Li, X. P. Ouyang, Z. Y. Wu, Q. Xu, *Phys. Chem. Chem. Phys.* **2020**, *22*, 6970.
- [67] S. H. Yang, C. Y. Lin, Y. M. Chang, M. J. Li, K. C. Lee, C. F. Chen, F. S. Yang, C. H. Lien, K. Ueno, K. Watanabe, T. Taniguchi, K. Tsukagoshi, Y. F. Lin, *ACS Appl. Mater. Interfaces* **2019**, *11*, 47047.
- [68] G. Mirabelli, C. McGeough, M. Schmidt, E. K. McCarthy, S. Monaghan, I. M. Povey, M. McCarthy, F. Gity, R. Nagle, G. Hughes, A. Cafolla, P. K. Hurley, R. Duffy, *J. Appl. Phys.* **2016**, *120*, 125102.



## Supporting Information

for *Small*, DOI: 10.1002/smll.202200913

Atomistic Observation of the Local Phase Transition in  
MoTe<sub>2</sub> for Application in Homojunction Photodetectors

*Yalan Wang, Miao Zhang, Zhongying Xue, Xinqian  
Chen, Yongfeng Mei, Paul K. Chu, Ziao Tian, Xing Wu,\*  
and Zengfeng Di\**

## Supporting Information

### **Atomistic Observation of the Local Phase Transition in MoTe<sub>2</sub> for Application to Homojunction Photodetector**

*Yalan Wang, Miao Zhang, Zhongying Xue, Xinqian Chen, Yongfeng Mei, Paul K. Chu, Ziao Tian, Xing Wu, \* and Zengfeng Di \**

## Supporting Section 1 : Sample preparation for *in situ* heating TEM observation

Other than the traditional TEM measurement, *in situ* heating TEM experiment was supported by the nano-chip, sample holder and a controller equipped with heating software (Digiheater). The nano-chip for *in situ* heating TEM experiment was supplied by DENS solutions. As shown in Supplementary Fig. 1a, there are few electrodes on the nano-chip, which are connected to the sample holder. Supplementary Fig. 1b-1c display two optical images of the nano-chip, the electrodes extend to surround the sample holding windows in order to transfer the setting temperature in the form of joule heating. The round and oval transparent silicon nitride membrane windows are used for holding the experimental samples, and Supplementary Fig. 1d is an image of the window containing few 2H MoTe<sub>2</sub> fragments under TEM observation in low magnification. The heating controller, connected with the sampler holder, was manipulated by a computer with heating software. The rate of the temperature ramping up and down is about 290 °C s<sup>-1</sup>.

The bulk 2H MoTe<sub>2</sub> was pulverized mechanically into small pieces and were placed in a 5 ml centrifuge tube. Ethanol was the ultrasonic solvent and the sample was sonicated for 30 min to cleave into fragments with a nanometer-scale thickness for TEM measurement. The supernatant liquid was dropped on the transparent silicon nitride membrane window of the nano-chip under an optical microscope and some MoTe<sub>2</sub> fragments were measured after ethanol evaporation. MoTe<sub>2</sub> was sensitive to oxygen and water vapor and so the sample was prepared in a glove box.<sup>[1, 2]</sup>

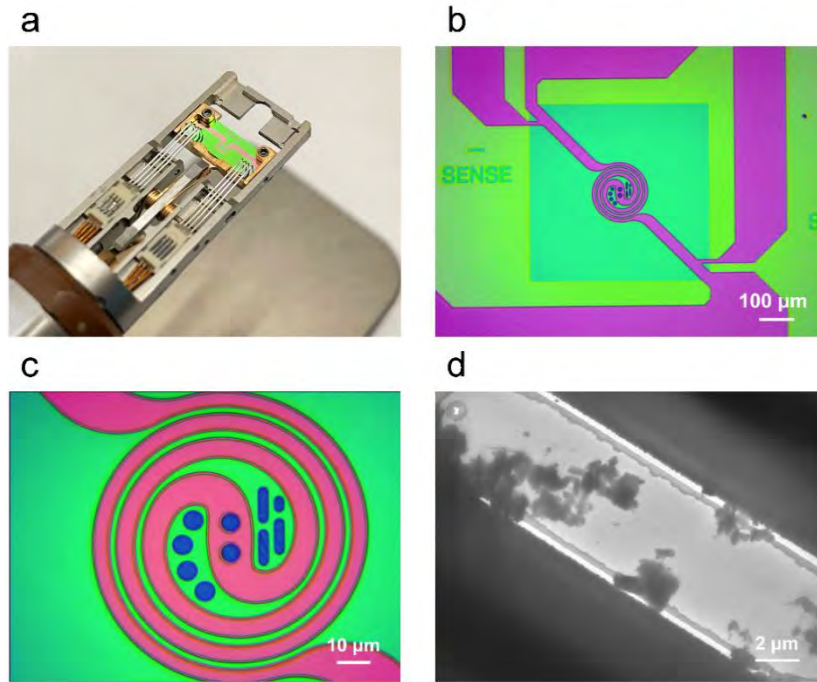


**Figure S1.** (a) Photo of the sample holder and the nano-chip for *in situ* heating TEM measurement. (b-c) Optical images of the nano-chip. (d) TEM image of the transparent silicon nitride membrane window with few samples on.

## Supporting Section 2: *In situ* heating TEM observation

*In situ* heating TEM was conducted at 80 kV on the aberration-corrected JEM-ARM300F with a heating holder and the heating progress was programmed to reach the target temperature from room temperature (20 °C) (Figure S2a, Supporting Information), then the temperature was set to 20 °C immediately after each heating pulse to acquire the micrograph. To avoid sublimation, the atomic structures and SEAD patterns were examined after each heating pulse at the gradually elevating temperature, and a vivid phase transition was acquired after a heating pulse at 880 °C. Due to sample drift at high temperature, there might be a little deviation in the observed sample edges, as shown in Figure S2b-g, Supporting Information. In Figure S2b-f, the fast Fourier transform (FFT) patterns confirm that there is no phase transition in the observed area as indicated by one single set of diffraction pattern. However, when the temperature reaches 880 °C, the morphology of MoTe<sub>2</sub> has partially changed, that is, from 2H phase to 1T' phase. The coexistence of 2H and 1T' phases is revealed by TEM image and the corresponding FFT pattern, which shows two sets of diffraction patterns, as displayed in Figure S2g. Morphologically, the heat-induced 1T' MoTe<sub>2</sub> domains had straight and staggered arrangements, as shown in Figure S2g, Supporting Information. According to previous studies, it could be attributed to the “wagon wheel” structures and inversion domain boundary (IDB) defects formed at a high temperature.<sup>[3,4]</sup>

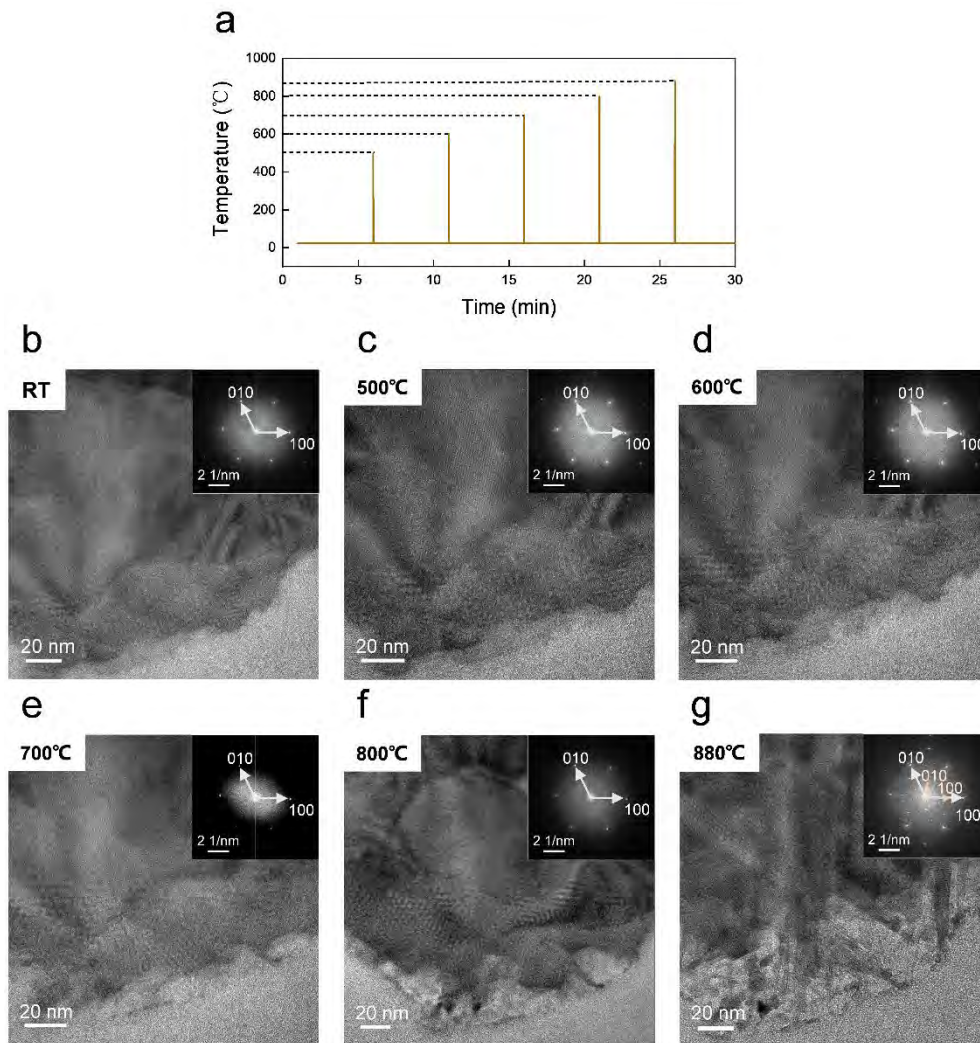


**Figure S2.** (a) Heating curves of *in situ* heating programs in the TEM measurement. (b) HR-TEM micrograph of the 2H MoTe<sub>2</sub> flake at room temperature. (c-g) HR-TEM micrographs of the 2H MoTe<sub>2</sub> flake after each heating pulse at different temperatures. No changes in the atomic arrangements or diffraction spots are observed until the temperature reaches 880 °C, at which the new ribbon-shape domains appear. The Miller indices corresponding to 2H MoTe<sub>2</sub> and 1T' MoTe<sub>2</sub> are denoted by white arrows and lightpink arrows in the inserted fast Fourier transform (FFT) patterns, respectively.

### **Supporting Section 3 : The seamless connection between 2H MoTe<sub>2</sub> and heat-induced 1T' MoTe<sub>2</sub>**

To obtain a distinct image of the interface of 1T' MoTe<sub>2</sub> and 2H MoTe<sub>2</sub>, HR-TEM was carried out to examine the phase transition area in Figure 1g. As shown in Figure S3, Supporting Information, the magnified region shows both the 1T' MoTe<sub>2</sub> and 2H MoTe<sub>2</sub> phases. The hexagonal lattice structure exists in 2H MoTe<sub>2</sub> area, while the monoclinic lattice structure is observed from the 1T' MoTe<sub>2</sub> region. The two phases are seamlessly stitched by covalent bonds, forming a coherent interface. Below the HR-TEM micrograph is the schematic illustration of the seamless interface between these two phases, showing the atomic arrangement in the stitched area (orange spheres are Mo atoms and blue spheres are Te atoms).



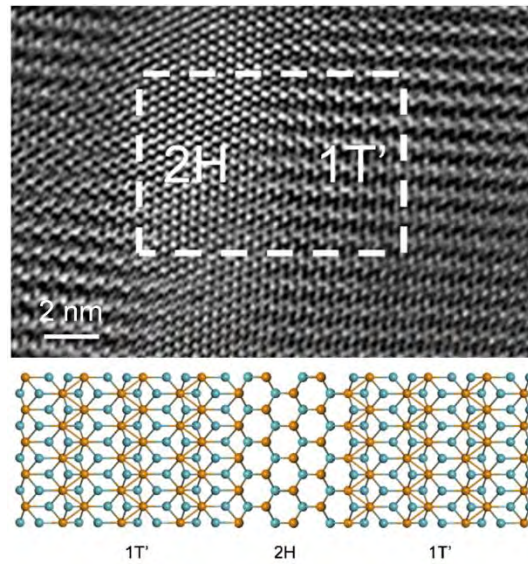


**Figure S3.** HR-TEM micrograph of MoTe<sub>2</sub> after a spike heating at 880 °C and the schematic illustration of the seamless interface. The coexistence of 2H MoTe<sub>2</sub> and 1T' MoTe<sub>2</sub> is observed and the interface between these two phases is focused by the dotted white box. The schematic illustration shows the microstructure of interface between 2H MoTe<sub>2</sub> and 1T' MoTe<sub>2</sub>, and orange and blue spheres represent Mo atoms and Te atoms, respectively.

#### **Supporting Section 4: Device fabrication and characterization**

To prevent contaminants from polymethyl methacrylate (PMMA) and electron beams, four parallel electrodes were prepared on the substrate. After electron beam lithography (EBL, Zeiss Sigma system), Cr/Au (5 nm/40 nm) was deposited by electron beam evaporation (EBE, Kurt J. Lesker). The electrodes were not too thick because MoTe<sub>2</sub> was fragile in the following transfer process. After lifting off, the substrate with markers and bottom electrodes was rinsed in acetone to remove residues to enable subsequent dry transfer of MoTe<sub>2</sub>. 2H MoTe<sub>2</sub> and h-BN were mechanically exfoliated down to thin layers in a glove box. To minimize potential pollution from air, the thickness of the exfoliated films was determined roughly by an optical microscope in the glove box before annealing. The PF gel films (Gel Pak) were used to transfer the desired 2H MoTe<sub>2</sub> and h-BN onto SiO<sub>2</sub>/Si on the substrates successively.

The sample was transferred to a furnace and annealed at 880 °C for 5 min. The furnace was kept at atmospheric pressure under 60 sccm H<sub>2</sub> and 10 sccm Ar. Compared to the suspended TEM grid, the thermal conductivity of the SiO<sub>2</sub>/Si substrate was better and therefore, the annealing time was extended in furnace annealing.<sup>[5]</sup> Afterwards, the device was instantly cooled down to room temperature under 500 sccm Ar and the phase transition occurred in the exposed MoTe<sub>2</sub> area. Raman scattering (HORIBA Jobin Yvon HR800) was performed on the device with a 514 nm excitation laser (Figure 3b and Figure S4a, Supporting Information). The feature peak corresponding to the covering h-BN appears at 1361.7 cm<sup>-1</sup>. The spot size of the Raman laser was 1 μm and the laser power was as low as 1 mW to avoid the laser-induced phase transition in MoTe<sub>2</sub>.<sup>[6]</sup> The thickness of the annealed device was measured by AFM (Bruker, Multimode 8) using the tapping mode (Figure S4b, Supporting Information). The thickness of the exfoliated MoTe<sub>2</sub> was ~8 nm which was sufficient for the phase transition prior to possible complete sublimation of the MoTe<sub>2</sub> flake. The thickness of the exfoliated h-BN was ~40 nm.

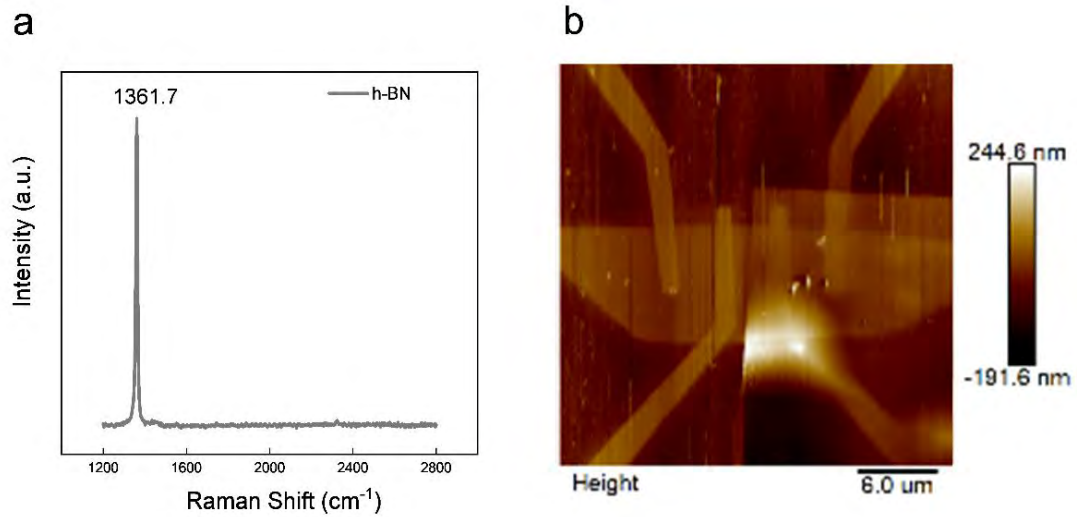


**Figure S4.** Device characterization. (a) Raman scattering spectrum of h-BN on the lateral 1T'-enriched MoTe<sub>2</sub>/2H MoTe<sub>2</sub> homojunction. (b) AFM topography of the lateral 1T'-enriched MoTe<sub>2</sub>/2H MoTe<sub>2</sub> homojunction. Two parallel electrodes are located below h-BN/MoTe<sub>2</sub>, while two other electrodes are located below the exposed MoTe<sub>2</sub>. The channel widths between the four electrodes are about the same (~3 μm).

## **Supporting Section 5: Cross-sectional TEM examination of the MoTe<sub>2</sub> homojunction**

Prior to focused ion beam (FIB) cutting, 150 nm thick Al was deposited to prevent high energy Ga ion bombardment of the device. FIB was performed on the Helios G4 UX. To avoid oxygen and water vapor, the sample with the freshly prepared cross-section was sealed after FIB processing. TEM was performed at 80 kV on the aberration-corrected JEM-ARM300F. Figure S5 in Supporting Information shows the cross-sectional TEM and EDS data of the 1T'-enriched MoTe<sub>2</sub>/2H MoTe<sub>2</sub> homojunction device.

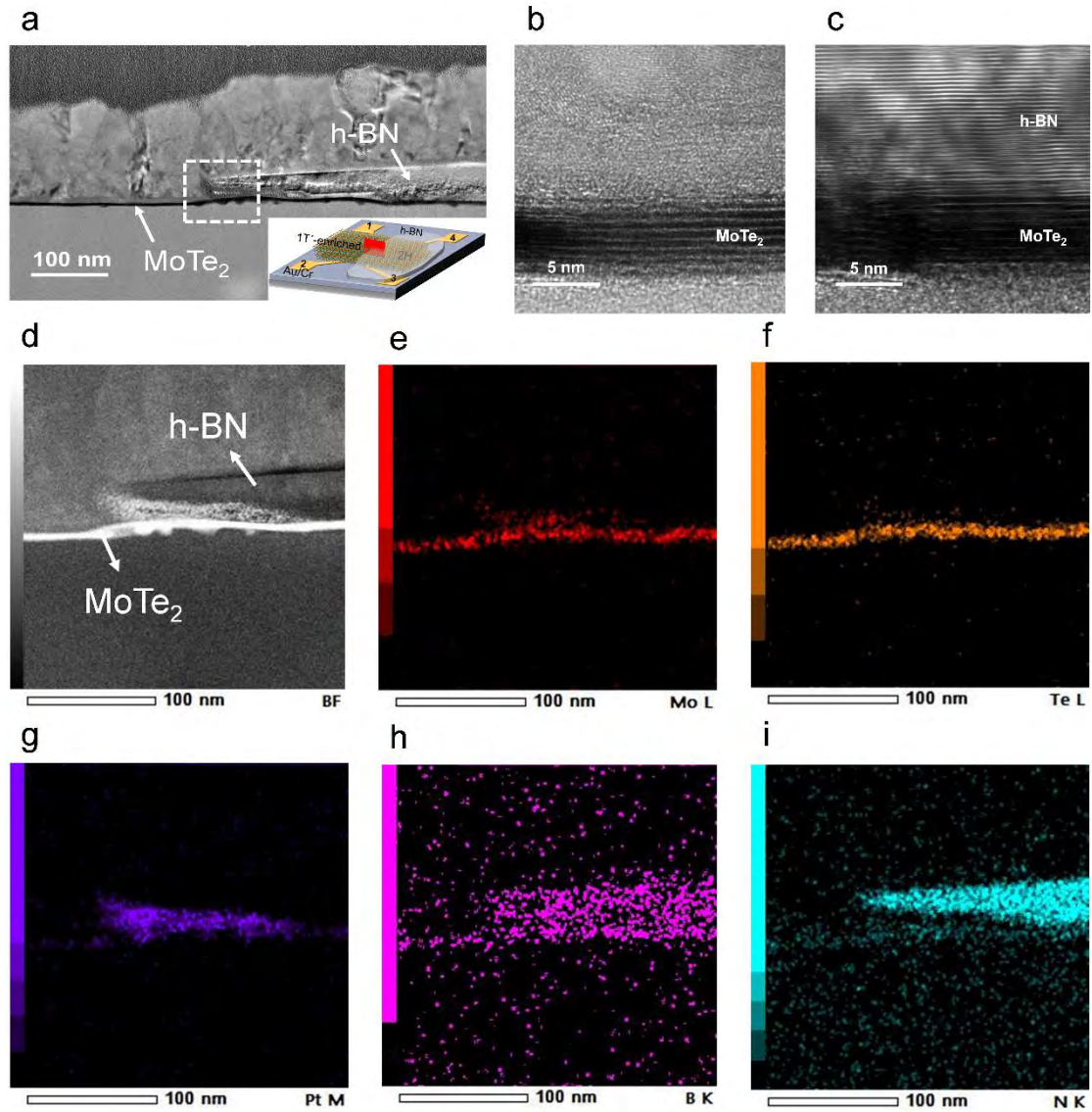


**Figure S5.** (a) Cross-sectional TEM image of the 1T'-enriched MoTe<sub>2</sub>/2H MoTe<sub>2</sub> homojunction with the red square in the inset showing the FIB region. (b, c) Cross-sectional TEM images of the regions corresponding to 1T'-enriched MoTe<sub>2</sub> and 2H MoTe<sub>2</sub> covered by h-BN respectively. The layered structure of MoTe<sub>2</sub> can be observed, and the thickness of the mechanically exfoliated MoTe<sub>2</sub> is ~8 nm. In the exposed area, there is compact Al above the MoTe<sub>2</sub> as the protecting layer in the FIB process. On the other side, MoTe<sub>2</sub> is in close contact with the layered h-BN. (d) Magnified area of the dotted white box in (a) showing the uneven thickness of the mechanically exfoliated h-BN. (e-i) EDS maps of Mo, Te, B and N for the panels in (e), (f), (h) and (i), respectively. (g) Nonuniform distribution of Pt originating from

FIB sample processing.

## Supporting Section 6:

**Table 1. Comparison of MoTe<sub>2</sub>-based photodetectors with different device layouts.**

Channel Material	Channel Structure	Rise time	Fall time	Responsivity and Detectivity	Reference
1T'-enriched MoTe <sub>2</sub> / 2H MoTe <sub>2</sub>	Homojunction	384 $\mu$ s	473 $\mu$ s	0.28 mA/W $2.8 \times 10^9$ Jones	This work
MoTe <sub>2</sub>	Homojunction	<2 ms	<2 ms	$160 \pm 3$ mA/W N. A.	[7]
MoTe <sub>2</sub> /Au	Heterojunction	<13 ms	<8 ms	5.07 A/W $6.34 \times 10^{11}$ Jones	[8]
MoTe <sub>2</sub> / Germanium	Heterojunction	5 ms	5 ms	12,460 A/W $3.3 \times 10^{12}$ Jones,	[9]
MoTe <sub>2</sub> / MoS <sub>2</sub>	Heterojunction	25 ms	Didn't mention	322 mA/W N. A.	[10]
MoTe <sub>2</sub> / Graphene	Heterojunction	78 ms	345 ms	970.82 A/W $1.55 \times 10^{11}$ Jones	[11]

## Supporting References

- [1] S. H. Yang, C. Y. Lin, Y. M. Chang, M. J. Li, K. C. Lee, C. F. Chen, F. S. Yang, C. H. Lien, K. Ueno, K. Watanabe, T. Taniguchi, K. Tsukagoshi, Y. F. Lin, *ACS Appl. Mater. Interfaces* **2019**, *11*, 47047.
- [2] G. Mirabelli, C. McGeough, M. Schmidt, E. K. McCarthy, S. Monaghan, I. M. Povey, M. McCarthy, F. Gity, R. Nagle, G. Hughes, A. Cafolla, P. K. Hurley, R. Duffy, *J. Appl. Phys.* **2016**, *120*, 125102.
- [3] H. Zhu, Q. X. Wang, L. X. Cheng, R. Addou, J. Y. Kim, M. J. Kim, R. M. Wallace, *ACS Nano* **2017**, *11*, 11005.
- [4] H. C. Diaz, Y. J. Ma, R. Chaghi, M. Batzill, *Appl. Phys. Lett.* **2016**, *108*, 191606.
- [5] Z. R. Chen, H. Y. Nan, Z. Liu, X. Y. Wang, X. F. Gu, S. Q. Xiao, *J. Raman. Spectrosc.* **2019**, *50*, 755.
- [6] S. Cho, S. Kim, J. H. Kim, J. Zhao, J. Seok, D. H. Keum, J. Baik, D. H. Choe, K. J. Chang, K. Suenaga, S. W. Kim, Y. H. Lee, H. Yang, *Science* **2015**, *349*, 625.
- [7] E. X. Wu, Y. Xie, S. J. Wang, D. H. Zhang, X. D. Hu, J. Liu, *Nano Res.* **2020**, *13*, 3445.
- [8] J. W. You, Y. Ye, K. Cai, D. M. Zhou, H. M. Zhu, R. Y. Wang, Q. F. Zhang, H. W. Liu, Y. T. Cai, D. Lu, J. K. Kim, L. Gan, T. Y. Zhai, Z. T. Luo, *Nano Res.* **2020**, *13*, 1636.
- [9] W. J. Chen, R. R. Liang, S. Q. Zhang, Y. Liu, W. J. Cheng, C. H. Sun, J. Xu, *Nano Res.* **2020**, *13*, 127.
- [10] A. Pezeshki, S. Hossein, H. Shokouh, T. Nazari, K. Oh, S. Im, *Adv. Mater.* **2016**, *28*, 3216.
- [11] W. Z. Yu, S. J. Li, Y. P. Zhang, W. L. Ma, T. Sun, J. Yuan, K. Fu, Q. L. Bao, *Small* **2017**, *13*, 1700268.